



## Estimates of wind energy input to the Ekman layer in the Southern Ocean from surface drifter data

Shane Elipot<sup>1,2</sup> and Sarah T. Gille<sup>1,3</sup>

Received 24 October 2008; revised 19 February 2009; accepted 24 March 2009; published 5 June 2009.

[1] The energy input to the upper ocean Ekman layer is assessed for the Southern Ocean by examining the rotary cross spectrum between wind stress and surface velocity for frequencies between 0 and 2 cpd. The wind stress is taken from European Center for Medium-Range Weather Forecasts ERA-40 reanalysis, and drifter measurements from 15 m depth are used to represent surface velocities, with an adjustment to account for the vertical structure of the upper ocean. The energy input occurs mostly through the nonzero frequencies rather than the mean. Phenomenologically, the combination of a stronger anticyclonic wind stress forcing associated with a greater anticyclonic response makes the contribution from the anticyclonic frequencies dominate the wind energy input. The latitudinal and seasonal variations of the wind energy input to the Ekman layer are closely related to the variations of the wind stress, both for the mean and for the time-varying components. The contribution from the near-inertial band follows a different trend, increasing from 30°S to about 45°S and decreasing further south, possibly a consequence of the lack of variance in this band in the drifter and wind stress data.

**Citation:** Elipot, S., and S. T. Gille (2009), Estimates of wind energy input to the Ekman layer in the Southern Ocean from surface drifter data, *J. Geophys. Res.*, 114, C06003, doi:10.1029/2008JC005170.

### 1. Introduction

#### 1.1. A Spectral View of the Wind Energy Input

[2] The transfer of mechanical energy from the atmosphere to the ocean takes place through a variety of physical mechanisms that can be distinguished by the timescales on which they occur. This study makes use of surface drifter data to examine the wind energy input to the Ekman layer on timescales ranging from low-frequency 40-day periods to near-inertial frequencies.

[3] First, at low frequencies, the wind stress  $\tau$  works on the ocean general circulation (represented by the geostrophic velocity  $\mathbf{u}_g$  at the surface) as:

$$\tau \cdot \mathbf{u}_g \equiv \mathbf{U}_e \cdot \nabla p_s / \rho. \quad (1)$$

equation (1) can be seen as either a direct generation of geostrophic kinetic energy or as an increase in potential energy by the work of the Ekman transport  $\mathbf{U}_e$  against the pressure forces at the surface  $\nabla p_s / \rho$  [Gill *et al.*, 1974; Fofonoff, 1981], with  $\rho$  the water density. Weijer and Gille [2005] showed that the potential energy framework is more germane to the energetics of a numerical model of the Southern Ocean. Wunsch [1998] estimated the left-hand side of equation (1) by using altimeter-derived geostrophic

velocities and wind stress field analyses for the 1992–1996 time period. In his estimate, 95% of wind energy input came from the time mean components of  $\tau$  and  $\mathbf{u}_g$ . Over the global ocean, the maximum energy input rates were greater than  $20 \times 10^{-3} \text{ W m}^{-2}$  and were found in the Southern Ocean (his Figure 2). Moreover, 70% of the wind work integrated over the surface of the global ocean was found south of 40°S. Huang *et al.* [2006] studied the decadal variability of this energy input from both altimeter data and numerical model output. They found that the ACC region is where most of the variability is concentrated for the 1979–2003 time period and furthermore that it is increasingly dominant in the global integral. More recent work has taken into account the influence of the current on the atmospheric stress [Duhaut and Straub, 2006; Hughes and Wilson, 2008]. Using extended observations, Hughes and Wilson [2008] updated Wunsch's estimates, reaching the same general conclusions, albeit with a decrease in the global integral because of the definite negative contribution to the wind work due to the effect of oceanic currents on atmospheric wind stress.

[4] Second, at high frequencies, near-inertial motions are triggered in the mixed layer by rapid wind stress fluctuations [e.g., D'Asaro, 1985b; Poulain, 1990]. Resonance can occur when the wind stress itself contains a significant rotary spectral component at the inertial frequency [e.g., Crawford and Large, 1996]. The energy flux at near-inertial frequencies has attracted interest, because it is potentially oriented downward toward the ocean interior by propagating internal waves [e.g., D'Asaro *et al.*, 1995]. These waves eventually dissipate and can drive diapycnal mixing [Gregg, 1987]. The energy flux to mixed layer near-inertial motions

<sup>1</sup>Scripps Institution of Oceanography, University of California, San Diego, La Jolla, California, USA.

<sup>2</sup>Now at Proudman Oceanographic Laboratory, Liverpool, UK.

<sup>3</sup>Department of Mechanical and Aerospace Engineering, University of California, San Diego, La Jolla, California, USA.

has been estimated from wind stress and ocean velocities measured at mooring locations [D'Asaro, 1985a] or more recently from global wind stress analyses [Alford, 2001; Watanabe and Hibiya, 2002; Alford, 2003a]. In these global studies, the inertial velocities  $\mathbf{u}_i$  were inferred from Pollard and Millard's [1970] damped slab-layer model for which the inertial currents are uniform in the vertical. By using either numerical integration in time of the equations of this model or solving them in the spectral domain, the wind energy input was computed as  $\boldsymbol{\tau} \cdot \mathbf{u}_i$ . Alford [2003a] also considered depth-uniform Ekman velocities  $\mathbf{u}_e$  arising from a time-varying Ekman transport, because their energy is also available for dissipation, but found their impact to be modest. For the period 1989–1995, the average zonal mean energy input rate at 40°S was about  $3 \times 10^{-3} \text{ W m}^{-2}$  (his Figure 1). However, this value may be too large since Plueddemann and Farrar [2006] showed that the slab-layer model systematically results in an overestimation of the work done on mixed layer inertial currents, largely because a slab model lacks dissipation on short timescales.

[5] Third, energy fluxes seem to take place at intermediate or “subinertial” frequencies through Ekman dynamics. Vertically sheared Ekman currents are expected to exist for all forcing frequencies according to Gonella [1972] “extensions” of Ekman's [1905] theory. He first derived several transfer functions that provide a mathematical representation of the wind-driven velocity as a function of depth and forcing frequency. Elipot and Gille [2009] studied the theoretical linear transfer functions arising from nine variants of the Ekman model, which differed in the parameterization of the vertical eddy viscosity and the boundary condition at the bottom on the wind-driven layer. Although these transfer functions vary in the details, in general, the predicted Ekman velocities  $\mathbf{u}_e$  spiral with depth from the surface and rotate along with the forcing wind stress vector. The transfer functions all predict a stronger response when the frequency of the forcing is anticyclonic (counterclockwise or positive in the Southern Hemisphere) than when it is cyclonic. They also exhibit either an unbounded or a maximum resonant response at the inertial frequency. While the Ekman currents themselves should play a role in the wind energy input into geostrophic currents via equation (1), maintaining the Ekman spiral requires dissipation within the Ekman layer, or a wind energy input rate “to the Ekman layer”. Elipot and Gille's [2009] results showed that the best models to explain drifter observations in the Southern Ocean have a bounded response at the inertial frequency at which there is a zero cross-wind component of the wind-driven velocity, and the wind energy input is therefore maximal.

[6] Wang and Huang [2004] estimated the wind energy input to the Ekman layer by using the transfer function to compute the ocean surface Ekman velocities  $\mathbf{u}_e$  from wind stress analyses, assuming that the Ekman model with a constant vertical viscosity and infinite depth ocean applied. They set the Ekman depth to be proportional to the mean friction velocity computed from the wind stress and inversely proportional to the Coriolis parameter. The total wind energy input into the Ekman layer was then obtained by summing the dot product  $\boldsymbol{\tau} \cdot \mathbf{u}_e$  over all frequency components. They found that the global integral for this energy input is also dominated by the contribution from the

Southern Hemisphere. Examination of Figure 3 in the paper by Wang and Huang [2004] reveals that this is mainly due to the strong winds over the Southern Ocean and notably large values over the ACC of about  $20 \times 10^{-3} \text{ W m}^{-2}$ . They also computed the changes of the global energy input to the Ekman layer over the 1948–2002 time period, which Huang et al. [2006] subsequently attributed to wind stress variability in the equatorial region and in the Southern Ocean.

## 1.2. Does the Wind Energy Input Into the Ekman Layer Matter?

[7] We will show in this paper that the observed cospectrum between wind stress and oceanic velocities as measured by drifters at 15 m is representative of a momentum flux from the atmosphere to the ocean. This flux takes place at a wide range of frequencies, from low to subinertial and inertial frequencies. The wind work on the geostrophic circulation is actually a source of mechanical energy for the interior ocean [Stern, 1975], but previous studies have not resolved how the wind works on ageostrophic motions, nor have they explained how the generation of ageostrophic motions leads to a transfer of mechanical energy to the ocean interior, well below the surface [Ferrari and Wunsch, 2008; Plueddemann and Farrar, 2006]. Thus one may ask if the third pathway for energy input described above, because of subinertial oscillations, is a relevant source for the energy needed to sustain global meridional overturning circulation.

[8] Von Storch et al. [2007] derived a mechanical energy budget for output from a high-resolution ocean general circulation model (OGCM) that represented vertical mixing with the nonlocal K-profile Parameterization (KPP) of Large et al. [1994]. Their analysis showed that the power provided by the wind at the sea surface was not separated between the work done on the geostrophic and ageostrophic circulation, because both components contributed to the total energy transferred down the water column. The dominant terms in the energy equation appear to be the pressure work and the shear-induced stress but the relative importance of these two terms was seen to vary as a function of depth. Overall, their results suggested that about 30% of the total wind energy input, through geostrophic and ageostrophic pathways, is passed through the interior ocean, while the remaining 70% is dissipated locally or converted to potential energy in the upper ocean. These results suggested that it is therefore necessary to estimate all pathways of wind energy input at the surface of the ocean.

[9] Von Storch et al. [2007] did not distinguish the inertial band contribution from the contribution due to Ekman dynamics at other frequencies. This is understandable, because the concept of a slab-layer at near-inertial frequencies is incompatible with the full primitive equations employed in an OGCM. Moreover, their model forcing had 1-day resolution and may have suppressed higher-frequency variability. In fact, theoretical analysis of internal wave generation by surface forcing [Gill, 1984], a recent numerical large eddy simulation [Polton et al., 2008], and observations [D'Asaro et al., 1995; Alford and Whitmont, 2007] all have shown that near-inertial processes are important in the ocean.

### 1.3. Estimates From in Situ Data in This Study

[10] In this study, we show how to isolate and estimate the wind energy input to the Ekman layer from in situ data. This approach merits attention, if only because the concept of wind energy input to the Ekman layer has led to several estimates previously mentioned [Wang and Huang, 2004; Huang et al., 2006] but none from in situ observations of oceanic velocities on large scales. At least locally, it complements other data-based estimates of the wind work through other energy pathways like the one through geostrophic motions [e.g., Wunsch, 1998]. We focus here on the Southern Ocean (rather than the global ocean), because as previous studies have noted, it is the primary region for wind forcing to drive the ocean, and this wind energy is therefore thought to contribute to wind-induced mixing needed to sustain the thermohaline structure of the world ocean [Wunsch and Ferrari, 2004].

[11] The steps leading to the development of the equations in this paper, their interpretation and the subsequent estimates were motivated by observations of wind-coherent subinertial motions in drifter data [Weller, 1981; McNally et al., 1989; Niiler and Paduan, 1995; Rio and Hernandez, 2003; Elipot, 2006]. This correlation as a function of frequency has now been explained quite clearly by the development of Ekman theory extensions [Gonella, 1972; Rudnick and Weller, 1993; Elipot and Gille, 2009].

[12] After describing the data, we show here typical wind stress and drifter velocity spectra (section 2). Next we derive a spectral energy equation and show that the wind energy input to the Ekman layer (i.e., the energy input in the oceanic boundary layer as represented by “Ekman” models) is equal to the real part of the cross spectrum between the ocean velocity at the surface and the atmospheric wind stress (section 3), and we show a proxy for this cross spectrum in the form of the cross spectrum between wind stress and drifter velocity.

[13] Because drifters are drogued at 15 m depth rather than following currents exactly at the ocean surface, some knowledge of the vertical structure of the transfer function is needed to obtain the cross spectrum at the surface, and some biases need to be considered. This is discussed in section 4. It is important to note that the results from Elipot and Gille [2009] are used to infer the cross spectrum at the surface and therefore to estimate the wind energy input to the Ekman layer zonally averaged in the Southern Ocean (section 5). The results are discussed in terms of spectral decomposition as well as latitudinal and seasonal variations. Section 6 provides a summary and concluding remarks.

## 2. Data and Their Spectra

### 2.1. Data

[14] Ideally, the cross spectrum mentioned in section 1.3 would be computed using time series of wind-driven velocity at the surface and contemporaneous wind stress time series, at fixed locations, on a regular grid over the world ocean. However, observations from moorings are too sparse to provide representative estimates on global scales, and their shallowest velocity measurement depths are usually too far from the surface. Instead, here we take advantage of velocity data derived from surface drifter trajectories. Drifter data are not ideal for obtaining the cross

spectrum at the surface, and our estimates suffer from nonnegligible uncertainties as well as some biases (discussed in section 4). Nonetheless, we show here that a first estimate from data in this region can be obtained and used as a benchmark for other indirect estimates. Such an estimate may eventually be refined as our understanding of Southern Ocean boundary layer dynamics improves.

[15] The ongoing Global Drifter Program (GDP) (previously known as the Surface Velocity Program (SVP)) provides horizontal velocity data from surface drifters on a global scale. The time period covered by the drifter data used in this study is from November 1992 to July 2002. A standard SVP drifter has a Holey-Sock drogue centered at 15-m depth, linked by a tether to a surface float that radio-transmits its positions to the ARGOS satellite array at uneven time intervals, depending on satellite coverage and the drifter’s setup [Lumpkin and Pazos, 2007]. The NOAA Atlantic Oceanographic and Meteorological Laboratory (AOML) processes the raw position data and interpolates them using a kriging procedure [Hansen and Poulain, 1996], resulting in a time series of positions at 6-hour intervals. Drifter trajectories used in this study are plotted in Figure 1. From these, velocities at the drifter positions were computed by using a forward difference scheme over 6 hours.

[16] The drifter ageostrophic velocities were then estimated by subtracting surface geostrophic velocities. For this, geostrophic velocities were derived from gradients of 7-day altimetric sea surface height anomalies [Centre National d’Etudes Spatiales, 1996], to which we added a time mean geostrophic velocity computed from GRACE satellite-derived dynamic topography [Tapley et al., 2005].

[17] For wind data, we use European Center for Medium-Range Weather Forecasts (ECMWF) ERA-40 Project reanalysis wind stresses [Simmons and Gibson, 2000] obtained from the Data Support Section of the Scientific Computing Division at the National Center for Atmospheric Research. ECMWF wind stresses are released on a Gaussian grid with resolution of  $1.125^\circ$  longitude by roughly  $1.125^\circ$  latitude at 6-hour sampling. These grids were linearly interpolated on the drifter positions to obtain contemporaneous time series of wind stress.

### 2.2. Spectral Content of Drifter Velocity and Wind Stress

[18] Before using the cross spectrum to linearly link wind stress and drifter velocity variability, we examine their autospectra. As in the paper by Elipot and Gille [2009], spectra were estimated as follows: in a given  $2^\circ$  latitudinal band, 40-day time series were identified for drifter velocity and for wind stress at the position of the drifter, with 50% overlap between consecutive trajectories. For each segment, a Hanning window was applied, and then the data were Fourier transformed to obtain a raw periodogram. All periodograms in each latitudinal band were averaged in order to obtain a smooth periodogram estimate of the spectrum. The frequency resolution is therefore  $40^{-1}$  cpd, and the Nyquist frequency is 2 cpd. Formal error bars for the spectra estimates were computed following Bendat and Piersol [1986], on the basis of the number of trajectory segments in each zonal band (See histogram inset in Figure 1). See Elipot and Gille [2009] for more details.

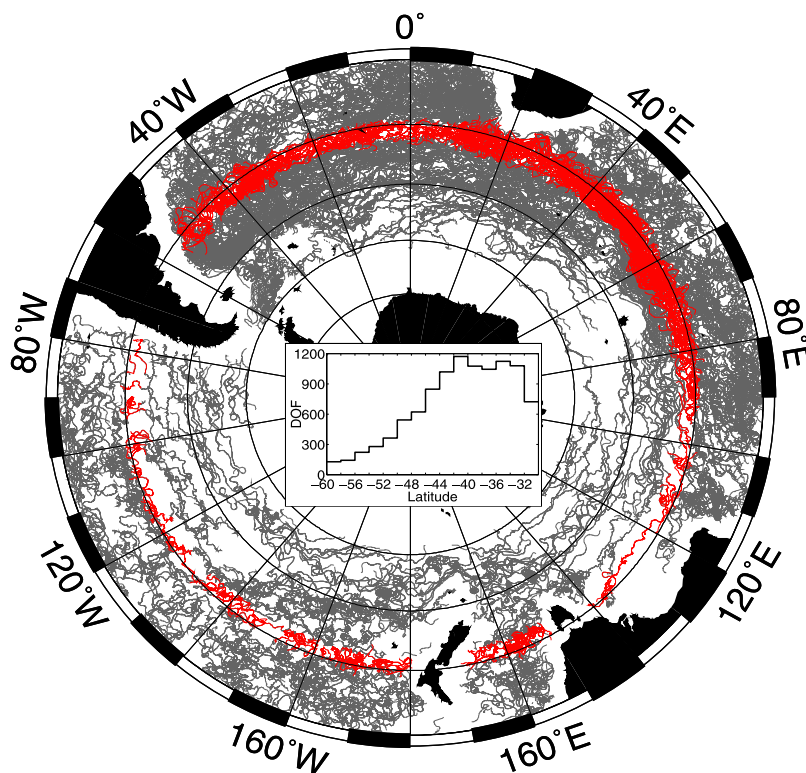


**Figure 1.** Surface drifter trajectory segments used in this study. The red segments correspond to the data in the 40° to 42° zonal band. The inset shows distribution of 20-day overlapping 40-day trajectory segments per 2° zonal band, which is also the number of degree of freedom (DOF) used for error bar estimates for spectra.

For illustrative purposes in this paper we show spectra derived from the data in the 40–42° zonal geographical band, but they are fairly typical of all the other zonal bands within the Southern Ocean.

### 2.2.1. Wind Stress Spectra

[19] The wind stress rotary autospectrum (heavy black lines in Figure 2) should be interpreted with care because this estimate does not formally represent a Lagrangian spectrum. It is not derived from material trajectories, and rather represents the wind stress forcing at drifter locations and measurement times. Such spectra has been computed and discussed before [e.g., *Rio and Hernandez, 2003; Elipot, 2006*]. Briefly, Figure 2 shows that the wind stress rotary spectrum is anticyclonically polarized [e.g., *Gonella, 1972*] which means that the anticyclonic spectrum (dashed lines) is higher than cyclonic spectrum (solid lines) for all corresponding frequencies considered. The anticyclonic and cyclonic spectra have the same red shape with an attenuation of about 10 dB per frequency decade. *Rio and Hernandez [2003]* interpolated ECMWF analysis wind surface stresses onto global SVP drifter positions and found similar features in their wind stress spectral estimates. Similarly, almost everywhere that moored buoy surface winds are available, *Stockwell et al. [2004]* found that anticyclonic spectral power exceeds cyclonic spectral power.

### 2.2.2. Ocean Velocity Spectra

[20] The Lagrangian rotary autospectrum from the drifter velocities is drawn with thin black lines in Figure 2. Both anticyclonic and cyclonic spectra are red in character, with a

gentler slope at low frequencies below about 0.1 cpd. The anticyclonic spectrum differs greatly from the cyclonic spectrum at high frequencies with a peak at about 1.3 cpd. This peak, ubiquitously reported in drifter data, corresponds to the anticyclonic motions in the ocean mixed layer occurring at the local inertial frequency [e.g., *Poulain, 1990; Poulain et al., 1992; Saji et al., 2000*]. Here, the inertial peak is broadened because of the latitudinal distribution of the data selected for this plot, and because of the latitudinal displacement of each 40-day trajectory segment. In contrast with the wind stress spectra, for the drifters the polarization of the spectrum is less pronounced and varies in character. Anticyclonic power predominates for all frequencies except here around 0.3 cpd where the polarization is marginally cyclonic. The polarization of oceanic rotary spectra at subinertial frequencies has previously been reported and is usually ascribed to coherent vortices rotating in different directions [e.g., *Lumpkin and Flament, 2001; Griffa et al., 2008; Elipot and Lumpkin, 2008*].

[21] The ageostrophic velocity rotary autospectrum is drawn with gray lines in Figure 2. For frequencies less than 0.1 cpd, this spectrum is much reduced compared to the drifter velocity spectrum. This suggests that at low frequencies, the geostrophic component dominates the drifter velocities. For frequencies greater than about 0.4 cpd, the ageostrophic and drifter velocity spectra are identical, as no geostrophic variance is expected in the AVISO data at these higher frequencies. The ageostrophic velocity spectrum is mostly polarized anticyclonically except at frequencies

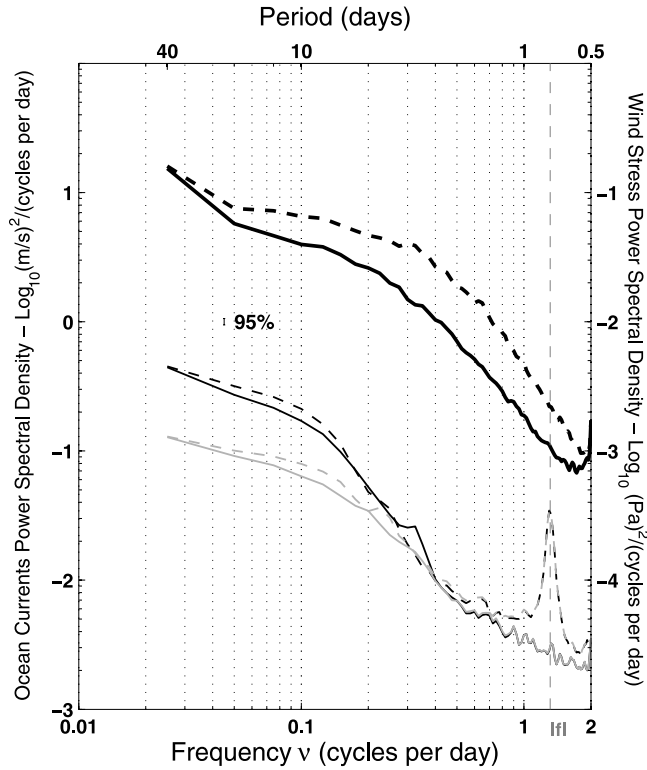


**Figure 2.** Spectral densities for stresses (heavy black curves; right ordinates axis) and drifter velocities (thin black curves) and ageostrophic velocities (thin gray curves; left ordinates axis) for the data in the  $40^\circ$  to  $42^\circ$  zonal band. Solid curves correspond to cyclonic frequencies, and dashed curves correspond to anticyclonic frequencies. The error bar is the formal 95% confidence interval for autospectral estimates based on the number of raw periodograms averaged to obtain the smooth spectral estimate in this latitude band. The vertical dashed line indicates the mean inertial frequency.

between approximately 0.3 cpd to 0.4 cpd. In this range, the polarization is not statistically different from zero anywhere. This suggests that the cyclonic polarization mentioned above for the drifter velocity spectrum can be ascribed to the geostrophic component of the drifter velocities. In contrast, the anticyclonic polarization of the ageostrophic spectra may be explained by the stronger anticyclonic wind forcing and by a preferential response of the wind-driven upper ocean to anticyclonic wind stress [Gonella, 1972; Elipot and Gille, 2009].

[22] While the autospectra indicate the frequency decomposition of the variability of the wind stress and of the ageostrophic velocity, the amount of covariability between the two should be given by the cross spectrum. In the next section, we describe a theoretical interpretation for the cross spectra, and in sections 4 and 5 we estimate it from data.

### 3. Spectral Energy Equation

[23] The cross spectrum between wind stress and ocean surface velocity serves as the primary diagnostic tool for this paper. The derivation of a spectral energy equation from

the horizontal momentum balance shows that the real part of the cross spectrum, the cospectrum, gives an estimate of the rate of wind energy input to the Ekman layer.

#### 3.1. Spectral Energy Equation: The Balance of Spectra

[24] The linearized horizontal momentum balance for the ocean in the absence of horizontal pressure gradients is:

$$\frac{\partial \mathbf{u}(t, z)}{\partial t} + i f \mathbf{u}(t, z) = \frac{1}{\rho} \frac{\partial \boldsymbol{\tau}(t, z)}{\partial z}, \quad (2)$$

where here  $\mathbf{u}$  is the horizontal velocity,  $z$  the depth negative downward,  $\boldsymbol{\tau}$  is the turbulent Reynolds stress. The finite Fourier transform  $\int_0^T (\cdot) \exp(-i2\pi\nu_k t) dt$  of equation (2) is:

$$i(2\pi\nu_k + f) \mathbf{U}_k(\nu_k, z) = \frac{1}{\rho} \frac{\partial \mathbf{T}_k(\nu_k, z)}{\partial z}, \quad (3)$$

where  $\mathbf{T}_k$  is the Fourier transform of  $\boldsymbol{\tau}$ . Multiplying equation (3) by  $\mathbf{U}_k^*$  and integrating from  $z < 0$  to the surface  $z = 0$  gives:

$$i\rho(2\pi\nu_k + f) \int_z^0 |\mathbf{U}_k|^2 dz = \int_z^0 \frac{\partial \mathbf{T}_k}{\partial z} \mathbf{U}_k^* dz. \quad (4)$$

Integrating by parts the right hand side yields:

$$\begin{aligned} & i\rho(2\pi\nu_k + f) \int_z^0 |\mathbf{U}_k|^2 dz \\ &= \mathbf{T}_k \mathbf{U}_k^* \Big|_{z=0} - \mathbf{T}_k \mathbf{U}_k^* \Big|_z - \int_z^0 \mathbf{T}_k \left( \frac{\partial \mathbf{U}_k}{\partial z} \right)^* dz. \end{aligned} \quad (5)$$

The first term on the right-hand side of equation (5) corresponds to the wind stress boundary condition at the surface. The second term vanishes when we let  $z$  go to  $-\infty$  to represent the base of the wind-driven layer where velocities and/or turbulent stresses vanish, and hence their Fourier transforms go to zero. Next, we apply to this equation the expected value operator and divide by the length of the observation  $T$  to form a spectral energy equation:

$$i(2\pi\nu_k + f)E + D = S_{\tau\mathbf{u}}, \quad (6)$$

where

$$E = \rho \int_{-\infty}^0 \frac{\langle |\mathbf{U}_k|^2 \rangle}{T} dz, \quad (7)$$

$$D = \int_{-\infty}^0 \frac{\langle \mathbf{T}_k \left( \frac{\partial \mathbf{U}_k}{\partial z} \right)^* \rangle}{T} dz, \text{ and} \quad (8)$$

$$S_{\tau\mathbf{u}} = \frac{\langle \mathbf{T}_k \mathbf{U}_k^* |_{z=0} \rangle}{T} \quad (9)$$

are estimates of the vertically integrated kinetic power spectral density of the Ekman layer, the vertically integrated

dissipated power spectral density in the Ekman layer, and the power cross spectrum between the wind stress and the ocean surface velocity. This equation does not give the rate of change of energy but rather the average balance among various power spectral quantities.

[25] Next, we assume that the turbulent stress  $\boldsymbol{\tau}$  is proportional to the vertical shear (following a classical diffusion model),

$$\frac{\boldsymbol{\tau}(t, z)}{\rho} = K(z) \frac{\partial \mathbf{u}(t, z)}{\partial z}. \quad (10)$$

The stress is aligned with the velocity vertical shear, implying that the vertical eddy viscosity  $K$  is real and independent of time. No additional assumptions are applied to  $K$ . The finite Fourier transform of equation (10) is:

$$\frac{\mathbf{T}_k}{\rho} = K \frac{\partial \mathbf{U}_k}{\partial z}. \quad (11)$$

[26] Substituting (11) into (8) gives

$$D = \int_{-\infty}^0 \rho K \frac{|\frac{\partial \mathbf{U}_k}{\partial z}|^2}{T} dz \quad (12)$$

which is a real and positive quantity. The power cross spectrum can be decomposed classically into real and imaginary parts:

$$S_{\boldsymbol{\tau}\mathbf{u}} = C_{\boldsymbol{\tau}\mathbf{u}} - i Q_{\boldsymbol{\tau}\mathbf{u}}, \quad (13)$$

where  $C_{\boldsymbol{\tau}\mathbf{u}}$  is the coincident spectrum (cospectrum) and  $Q_{\boldsymbol{\tau}\mathbf{u}}$  is the quadrature spectrum (quad-spectrum). Thus, equation (6) splits into two equations:

$$D = C_{\boldsymbol{\tau}\mathbf{u}}, \quad (14)$$

$$-(2\pi\nu + f)E = Q_{\boldsymbol{\tau}\mathbf{u}}. \quad (15)$$

Equation (14) describes the throughput of energy in each frequency band: the dissipated energy in the Ekman layer (i.e., the energy sink) equals the energy source given by the cospectrum of the Ekman velocity at the surface and the wind stress. Equation (15) states that the kinetic energy of the Ekman layer can be obtained from the quad-spectrum. These equations resemble the spectral equations for atmospheric motions derived in the time domain by *Chiu* [1970], who found that the spectral density of the kinetic energy is shaped by quadrature spectral quantities and that the Coriolis parameter plays a role, as is apparent in equation (15).

### 3.2. Total Energy Input Rate to the Ekman Layer

[27] The Wiener-Khinchine theorem states that the frequency integral of the cross spectrum is equal to the complex cross-correlation function at zero time lag  $\mathbf{R}_{\boldsymbol{\tau}\mathbf{u}}(0)$  [e.g., *Bendat and Piersol*, 1986]:

$$\int_{-\infty}^{+\infty} S_{\boldsymbol{\tau}\mathbf{u}}(\nu) d\nu = \mathbf{R}_{\boldsymbol{\tau}\mathbf{u}}(0) \quad (16)$$

$$= \langle (\boldsymbol{\tau} - \langle \boldsymbol{\tau} \rangle)(\mathbf{u} - \langle \mathbf{u} \rangle)^* \rangle + \langle \boldsymbol{\tau} \rangle \langle \mathbf{u}^* \rangle. \quad (17)$$

For the real part this gives:

$$\int_{-\infty}^{+\infty} C_{\boldsymbol{\tau}\mathbf{u}}(\nu) d\nu = \mathcal{R}[\langle (\boldsymbol{\tau} - \langle \boldsymbol{\tau} \rangle)(\mathbf{u} - \langle \mathbf{u} \rangle)^* \rangle] + \mathcal{R}[\langle \boldsymbol{\tau} \rangle \langle \mathbf{u}^* \rangle], \quad (18)$$

which states mathematically that the integrated cospectrum equals the real part of the complex covariance of  $\boldsymbol{\tau}$  and  $\mathbf{u}$  plus the product of their time means. This does not imply that the cospectrum is the frequency distribution of the total work done on the ocean by the wind stress. The spectral analysis of the latter quantity would include the work on geostrophic currents and other processes including non-linear forcings and interactions between frequencies.

## 4. On Obtaining the Surface Cross Spectrum From Drifter Data

### 4.1. Shear Bias

[28] Drifter velocities are interpreted as 15 m velocities so that the cross spectrum with the wind stress is not the quantity that we seek to estimate in equation (9), and a correction for this shear bias needs to be implemented. At subinertial frequencies, a model with vertical shear for wind-driven velocity is preferable to a slab model [e.g., *Weller and Plueddemann*, 1996; *Elipot and Gille*, 2009]. In the spectral domain, the transfer function theoretically links the auto-spectrum of the wind stress to the cross spectrum of the wind stress and the velocity at depth  $z$  [*Elipot and Gille*, 2009]:

$$S_{\boldsymbol{\tau}\mathbf{u}}(\nu, z) = \mathbf{H}(\nu, z) S_{\boldsymbol{\tau}\boldsymbol{\tau}}(\nu). \quad (19)$$

The real part of (19) is:

$$C_{\boldsymbol{\tau}\mathbf{u}}(\nu, z) = \mathcal{R}[\mathbf{H}(\nu, z)] S_{\boldsymbol{\tau}\boldsymbol{\tau}}(\nu) \quad (20)$$

Applying this expression for  $z = 0$  and  $z = -15$ , the depth of a drifter's drogue, the cospectrum of the wind stress and the ocean velocity is:

$$C_{\boldsymbol{\tau}\mathbf{u}}(\nu, 0) = \frac{\mathcal{R}[\mathbf{H}(\nu, 0)]}{\mathcal{R}[\mathbf{H}(\nu, -15)]} C_{\boldsymbol{\tau}\mathbf{u}}(\nu, -15) \quad (21)$$

$$= R \times C_{\boldsymbol{\tau}\mathbf{u}}(\nu, -15). \quad (22)$$

$R$  is a shear correction coefficient which depends on frequency and that can be derived from the transfer function  $\mathbf{H}$ . *Elipot and Gille* [2009] estimated the transfer function from the same drifter and wind stress data used in this study. They fitted these observed transfer functions to analytic transfer functions that used different expressions for the oceanic boundary layer and for vertical viscosity and then sought best estimates of viscosity and boundary layer parameters in order to minimize misfit between observations and theory. They found that the overall best model across the Southern Ocean is a one-layer model with a

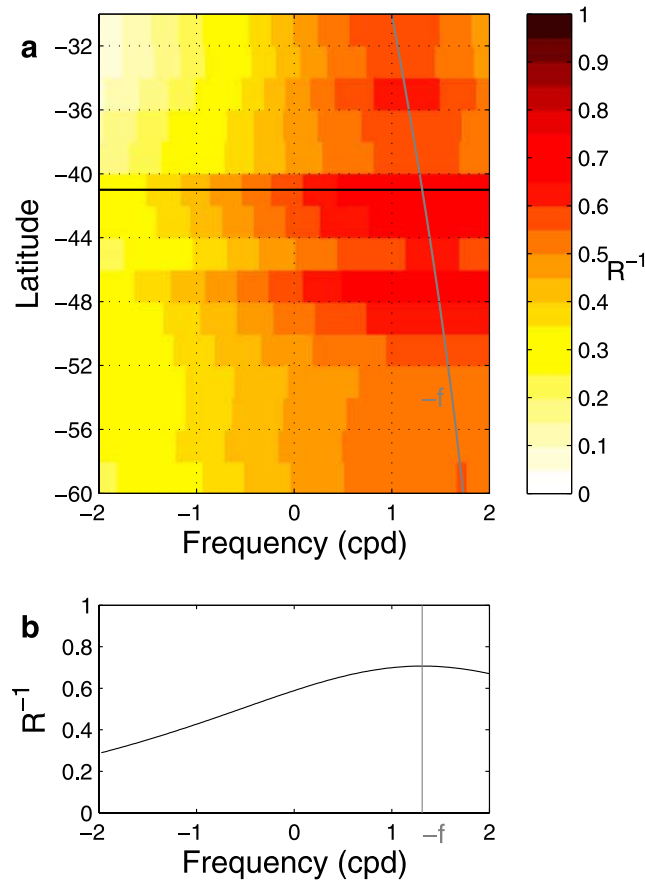


**Figure 3.** (a) Ratio of the cospectrum at 15 m to the cospectrum at the surface derived from the results of *Elipot and Gille* [2009]. The  $-f$  gray line indicates the inertial frequency as a function of latitude. (b) Ratio for the data in the  $40\text{--}42^\circ$  zonal band. The  $-f$  vertical line indicates the inertial frequency. Positive (negative) frequencies are anticyclonic (cyclonic).

constant viscosity  $O(0.01\text{--}0.1)\text{ m}^2\text{ s}^{-1}$  and a boundary layer depth  $O(30\text{--}50)$  m, with latitudinal variations. Here we use the parameters from this model to compute  $R$  to obtain the cospectrum at the surface by equation (21).

[29] Theoretically,  $1/R$  is less than one and more convenient to plot. Figure 3 shows  $1/R$  as a function of latitude and frequency from the results of *Elipot and Gille* [2009].

#### 4.2. An Example of Cross Spectrum at $41^\circ\text{S}$

[30] Figure 4 shows the cospectra and quad-spectra,  $C_{\tau u}$  and  $Q_{\tau u}$ , between the wind stresses and the ageostrophic velocities for the data in the  $40\text{--}42^\circ$  zonal band, but this plot is typical of the data set across the Southern Ocean. Note that for this plot, the cross spectrum has been corrected for a spurious time lag discussed in detail by *Elipot and Gille* [2009], and the shear bias described in the previous section has been corrected.

[31] Figure 4 indicates that the anticyclonic  $C_{\tau u}$  and  $Q_{\tau u}$  (dashed curves) both decrease by an order of magnitude and their cyclonic counterparts (solid lines) by two orders of magnitude, as frequency increases from  $(40)^{-1}$  to 1 cpd.  $C_{\tau u}$  and  $Q_{\tau u}$  are greater for anticyclonic than for cyclonic

subinertial frequencies. This suggests that the combination of a greater anticyclonic forcing spectra (Figure 2) and of a preferential anticyclonic ocean response [e.g., *Gonella*, 1972; *Elipot and Gille*, 2009] results in a greater dissipation  $D$  in the anticyclonic domain. This also suggests that the polarization of  $E$ , the kinetic power of the Ekman currents, is also anticyclonic and implies that more anticyclonic energy is present in the Ekman layer. Physically, this means that subinertial oscillations forced by the wind stress rotate anticyclonically.

[32] The inset in Figure 4 shows the 1 to 2 cpd frequency range.  $Q_{\tau u}$  approaches zero near the local inertial frequency and changes sign, in theoretical agreement with equation (15). At exactly the inertial frequency, the quad-spectrum is undefined. In cross-spectral analysis, the quad-spectrum indicates the amount of covariance that is in quadrature, that is  $90^\circ$  out of phase. For the case of the two vector quantities considered here (the wind stress and the ageostrophic velocity), the phase can be interpreted geometrically. When the quad-spectrum is zero the wind-coherent part of the oceanic velocity is aligned with the inertially rotating wind stress vector. Above the inertial frequency, the quad-spectrum changes sign since the wind-driven oceanic velocity is now located to the right of the wind vector, and no longer to the left of the wind stress vector. (Recall that in the Southern Hemisphere the mean Ekman current is to the left of the wind.) Further details about the geometric interpretation of the cross spectrum can be found in the papers by *Elipot* [2006] and *Elipot and Gille* [2009].

#### 4.3. Slip Bias

[33] Surface drifters are slightly imperfect water followers, and their measurements include an erroneous slip velocity thought to be caused by two phenomena: First, the direct action of the wind on the surface flotation buoy, and second the vertical shear of the horizontal velocity across the vertical extent of the drogue. *Niiler et al.* [1995] estimated the slip  $\mathbf{u}_s$  using vector measuring current meters mounted on the top and bottom of the drogues for a select group of drifters released in the tropical and northeastern Pacific. They modeled the slip as:

$$\mathbf{u}_s = \frac{a}{A} \mathbf{w}_{10} + \frac{b}{A} \Delta \mathbf{u}, \quad (23)$$

where  $\mathbf{w}_{10}$  is the 10-m wind velocity,  $A$  is the drag area ratio of the drogue to the other constituents of a drifter (40 for a SVP-type drifter) and  $\Delta \mathbf{u}$  is the velocity difference measured between the top and bottom of the drogue. Since  $\Delta \mathbf{u}$  cannot be determined from drifter data alone, here we do not attempt to evaluate the second term in (23). To estimate the impact of the first term in (23), we correct drifter velocities for wind slip using  $a = 4.63 \times 10^{-2}$  [*Niiler et al.*, 1995] and determining  $\mathbf{w}_{10}$  from ECMWF 10-m winds interpolated in space and time to drifter locations. As noted by *Niiler et al.* [2003], the wind slip correction may be underestimated in the Southern Ocean, where mean wind speeds often exceed  $10\text{ m s}^{-1}$ , the upper limit for which estimates of  $a$  have been validated.

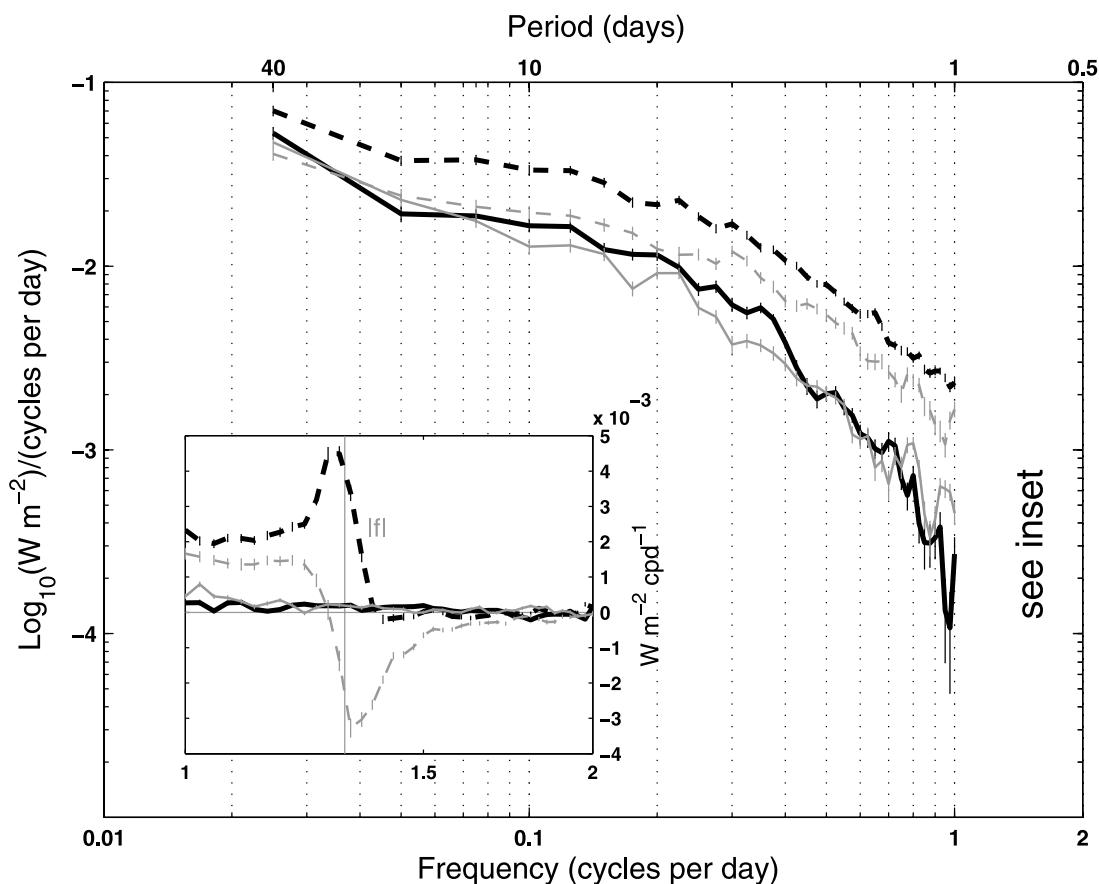


**Figure 4.** Surface cospectrum (heavy black curves) and quad-spectrum (light gray curves) density functions for anticyclonic (dashed curves) and cyclonic (solid curves) frequencies, on logarithmic scales between the wind stresses and the ageostrophic velocities for the data in the  $40^\circ$  to  $42^\circ$  zonal band. The inset enlarges the 1 to 2 cpd frequency range on linear scales. Error bars are the standard error of the means in each frequency band for the smoothed periodogram spectral estimate. Zero-frequency estimates are not plotted.

[34] The basic impact of this slip correction is to modify the estimates of the cross spectrum, but it potentially acts at two steps of the wind energy input computation. First, *Elipot and Gille* [2009] found that applying the wind slip correction tends to increase the magnitude of the vertical viscosity and of the boundary layer depth. This in turn reduces the shear from the surface to 15 m depth. Second, the wind slip correction also reduces the magnitude of the cospectrum and increases the quad-spectrum. Correspondingly, this reduces the inferred cospectrum of the wind stress and the surface ocean velocity after applying the shear correction. Finally, the estimates for the energy input rate  $D$  are accordingly reduced.

[35] We decided not to apply the wind slip correction to the drifter velocities. This decision draws from the probable inadequacy of the correction by *Niiler et al.* [1995] for regions of the world ocean with persistent high winds. However, in the next section we will consider the sensitivity of our results to the wind slip correction (see Figure 6a). The reduction to the energy input varies between approximately 10 and 40% across the Southern Ocean. These potential biases might seem large, but the fact that the results can be determined to better than  $\pm 50\%$  is a note-

worthy achievement for a first estimate of this type of wind energy input from in situ data. The presence of uncertainty in the estimates clearly calls for further research into the dynamics of the boundary layer as well as the behavior of surface drifters in high-wind environments.

## 5. Results and Discussion

[36] To summarize the method, for each  $2^\circ$  latitudinal band, we compute the cospectrum at 15 m, estimate the surface cospectrum following equation (21), and then sum the surface cospectrum over the frequency range resolved in this study (from  $-2$  cpd to  $2$  cpd) to obtain the wind energy input following the left-hand side of equation (18).

[37] At this stage the reader may wonder why we do not simply compute the cross covariance between  $\tau$  and  $\mathbf{u}$ , that is the right-hand side of equation (18). The first reason is that the shear correction depends on the frequency of the motions (as shown clearly by Figure 3) and cannot be applied to only the cross covariance, as pointed out by *Crawford and Large* [1996]. Second, by retaining the frequency information we gain a useful diagnostic of the

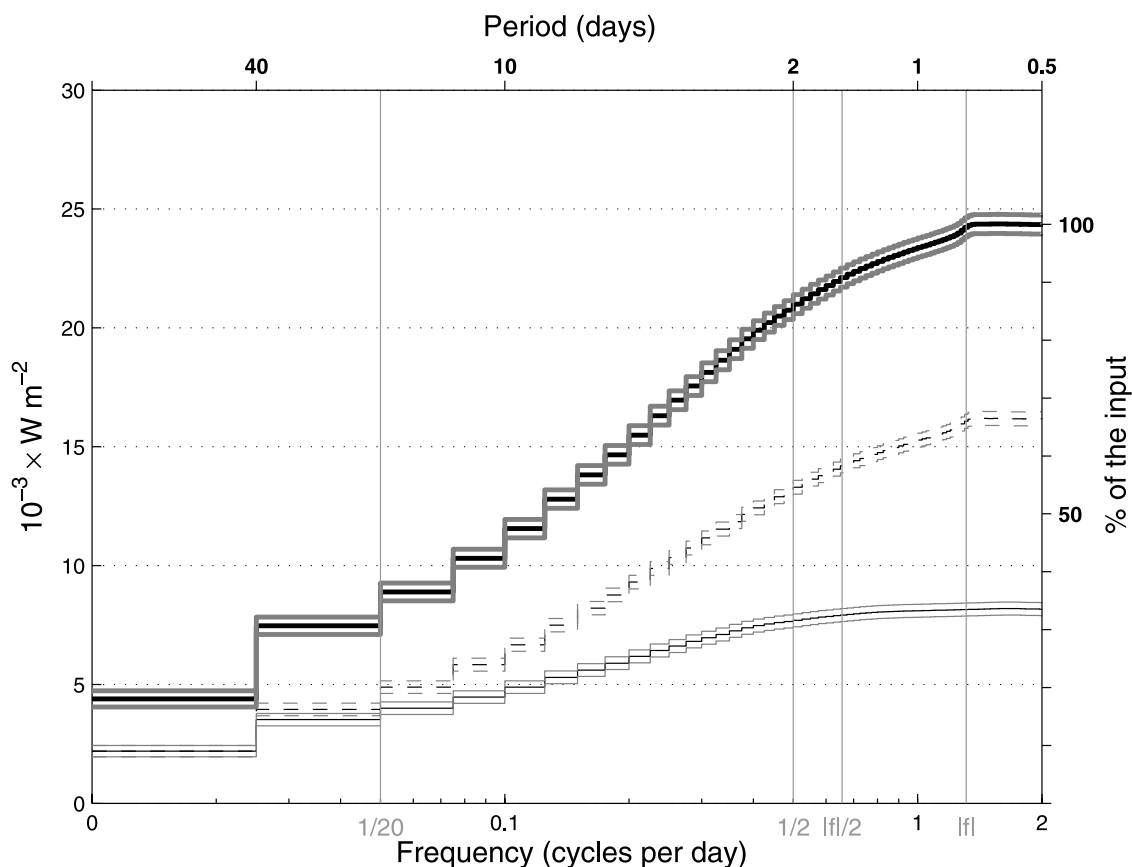


**Figure 5.** Cumulative integration of the surface cospectra at  $41^{\circ}\text{S}$  for anticyclonic frequencies (dashed curve), cyclonic frequencies (thin solid curve), and the sum of anticyclonic and cyclonic frequencies (solid heavy curve). Error bars are displayed as gray lines above and below each curve and are computed by propagating errors from the cospectrum. The axis of the abscissas is on a logarithmic scale, but the lowest frequency plotted in each case is the zero-frequency contribution, which is split evenly between the anticyclonic and cyclonic domains. Vertical lines mark specific frequencies.

frequencies that matter for the process under scrutiny, as will be shown in section 5.1.

### 5.1. Frequency Decomposition of the Input

[38] For the  $2^{\circ}$  latitudinal band centered at  $41^{\circ}\text{S}$ , Figure 5 shows the cumulative integration from frequencies 0 to 2 cpd of the surface cospectrum. Three summations are shown, one for anticyclonic frequencies (dashed curve), one for cyclonic frequencies (thin solid curve) and finally for both frequencies (heavy solid curve). The results in all other latitudinal bands are fairly similar to what is observed at  $41^{\circ}\text{S}$ .

[39] Anticyclonic frequencies contribute more to the total energy input than do the cyclonic frequencies, and this is true for all frequency ranges of summation greater than zero. This is due to a greater anticyclonic wind stress forcing reinforced by a greater anticyclonic response [Elipot and Gille, 2009]. This is a potential explanation for the predominance of anticyclonic “spin” in the Southern Ocean at these latitudes as revealed by Griffa *et al.* [2008].

[40] Time-varying components dominate the energy input relative to the zero-frequency contribution. Motions at frequencies higher than  $(20)^{-1}$  cpd actually generally contribute to more than about 50% of the total. The time-

varying nature of the wind energy input to the Ekman layer differs in this way from the wind work on geostrophic motions, which occur mostly through the mean [Wunsch, 1998; Hughes and Wilson, 2008] while the time-varying components up to  $(20)^{-1}$  cpd contribute only a few percent to the total.

[41] Here we can compare our results to Wang and Huang’s [2004] theoretical approach. Their estimates of the wind energy input to the Ekman layer varied between approximately 12 and  $20 \times 10^{-3} \text{ W m}^{-2}$  in the ACC region (see their Figure 3) but considered only contributions from frequencies up to 0.5 cpd. For our estimates the contribution from this same frequency range (see vertical gray line in Figure 5) are generally larger, here  $21 \pm 0.5 \times 10^{-3} \text{ W m}^{-2}$  at  $41^{\circ}\text{S}$  in Figure 5 with a maximum of  $49 \pm 2.6 \times 10^{-3} \text{ W m}^{-2}$  at  $57^{\circ}\text{S}$  (not shown). For their estimates Wang and Huang [2004] used a theoretical model to compute the Ekman velocities at the surface which assumes an infinitely deep ocean and a constant vertical viscosity. Elipot and Gille [2009] found this model to be the least successful of 9 simple models of the Ekman layer in the Southern Ocean. For the purpose of estimating the wind energy input, we speculate that Wang and Huang’s [2004] model underestimates the cospectrum because it requires that the veloc-

ities at the surface be directed  $45^\circ$  from the wind stress direction. Also, we find that higher frequencies from 0.525 to 2 cpd, add a nonnegligible contribution, here about  $3.3 \pm 0.8 \times 10^{-3} \text{ W m}^{-2}$  at  $41^\circ\text{S}$  or about 14% of the total. Overall, the contribution for frequencies higher than 0.5 varies between 9% and 15% for the latitudes considered here. Since the variance of the wind stress from numerical weather reanalyses and high-frequency drifter motions may be undersampled at high latitudes, the contribution from these frequencies may be even larger.

[42] The underestimate of the high-frequency variance is even more problematic in the “near-inertial” frequency range, here taken from half the inertial frequency to 2 cpd. The near-inertial input is found here to be  $1.98 \pm 0.03 \times 10^{-3} \text{ W m}^{-2}$  at  $41^\circ\text{S}$ , 8% of the total. Over the Southern Ocean as a whole, this percentage varies from 2.7% to 8.7% and is typically the same order of magnitude as the energy flux into wind-forced near-inertial mixed layer motions over broad oceanic regions, as estimated from a slab-layer model [e.g., Alford, 2001]. These numbers imply that at least for the Southern Ocean, the wind energy is input to the Ekman layer predominantly at subinertial frequencies and not in the inertial band. However, the contribution of the near-inertial frequency range is likely underestimated in these data sets. *Elipot and Lumpkin* [2008] suggest that much more energy is present in this band when the raw drifter data set is used compared to the historical 6 hourly kriged data set. The exact magnitude of this difference is difficult to assess, since the data sets used in this study and in the paper by *Elipot and Lumpkin* [2008] span different time periods. Moreover, a definite answer to this uncertainty in the contribution of high frequencies at high latitude for the energy input rate in the Ekman layer is not likely to be accessible until higher temporal wind information (that is higher-frequency sampling than 6 hours) is available.

## 5.2. Year-Round Data

[43] In order to study latitudinal and seasonal variability, cumulative integrals of cospectra such as those in Figure 5 were computed for each  $2^\circ$  latitudinal band between  $30^\circ\text{S}$  and  $60^\circ\text{S}$ . Energy input was summed separately for time mean and time-varying components, for anticyclonic and cyclonic components, and for the near-inertial frequency band. Figure 6 shows results for the year-round data set, and Figure 7 shows results for austral winter and summer.

[44] The total energy input rate is plotted in black in Figure 6a. It differs by more than a factor of 5 across the Southern Ocean, ranging from a minimum of  $(10 \pm 0.25) \times 10^{-3} \text{ W m}^{-2}$  at  $31^\circ\text{S}$  to a maximum of  $(55 \pm 2.6) \times 10^{-3} \text{ W m}^{-2}$  at  $57^\circ\text{S}$ . We split the total energy into contributions from the mean, or zero frequency, (blue line) and contributions from the time-varying components (red line). Both generally increase from north to south, the mean by more than a factor of 10 and the time-varying contribution by more than a factor of 5. Figure 6b shows that their relative contributions are comparatively consistent at all latitudes, with the mean having its most significant impact at  $51^\circ\text{S}$ , where it accounts for 27% of wind energy input. Wind stress, shown in Figure 6c is largest at  $53^\circ\text{S}$  for the mean (blue), the variance (red), and the total (black).

[45] Figure 6d shows the energy input rate to the Ekman layer split into cyclonic and anticyclonic frequencies. It is

predominantly anticyclonic at almost all latitudes in the Southern Ocean, except southward of  $57^\circ\text{S}$  where roughly an equal amount of energy is input through cyclonic and anticyclonic frequencies. The relative contributions of the anticyclonic and cyclonic frequencies are plotted in Figure 6e: the anticyclonic contribution decreases from 72% at  $31^\circ\text{S}$  to 50% at  $59^\circ\text{S}$ . (For this plot, the contribution of the mean is partitioned equally between the two frequency domains.) This anticyclonic predominance is a consequence of two factors. First, as shown in Figure 6f, the mean-squared wind stress forcing is larger for anticyclonic frequencies (dashed lines) than for cyclonic frequencies (solid lines) across the Southern Ocean. (The mean-squared wind stress  $\langle \tau^2 \rangle$  is about 70% anticyclonic frequencies at  $31^\circ\text{S}$ , decreasing to about 53% anticyclonic at  $59^\circ\text{S}$  (not shown).) Second, if the oceanic response were flat, then the ocean currents would exactly reflect the partitioning of the wind. Instead, here the ocean response is more strongly anticyclonic, because of the preferential anticyclonic response of the ocean, as predicted by theoretical Ekman models [*Elipot and Gille*, 2009].

[46] The third row of Figure 6 shows the impact of near-inertial frequencies taken from  $-f/2$  to 2 cpd. In Figure 6g, the energy input rate in near-inertial frequency range (gray line, here multiplied by 10 for legibility) increases with latitude, peaks at  $45^\circ\text{S}$  and decreases further south. Similarly, in Figure 6i, the variance of the near-inertial wind stress (gray, again multiplied by 10 for legibility) increases from  $31^\circ\text{S}$  to  $45^\circ\text{S}$ , then stays almost constant to  $53^\circ\text{S}$ , and finally decreases toward  $59^\circ\text{S}$ . The relative importance of the near-inertial to noninertial frequencies (Figure 6h) is quite modest, always less than 9%. The contribution from the near-inertial band is somewhat surprising. Why does the contribution from the near-inertial frequencies peak at latitudes to the north of the contribution from all the nonzero frequencies? There may be two reasons for this drop in the cospectrum as hinted earlier: first the low variance in ECMWF wind stress at higher latitudes [*Gille*, 2005], and second the drop of variance in the inertial band for drifter data toward higher latitudes because of the 6-hour interval used for computing drifter velocities which approaches the local inertial frequency [*Lumpkin and Pazos*, 2007; *Elipot and Lumpkin*, 2008].

## 5.3. Seasonal Variability

[47] The wind energy input rate estimates were recomputed after sorting the data between a summer season and a winter season. In general, the seasonal variability manifests itself latitudinally and also as a function of the frequency range considered.

[48] From summer to winter, south of  $48^\circ\text{S}$ , the energy input rates from the mean (light blue and light red lines in Figure 7a) are not distinguishable within the error bars. North of this latitude the differences are statistically significant except at  $31^\circ\text{S}$ . The energy input rates from the nonzero frequencies (dashed medium blue and red lines) increase by 69% on average from summer to winter. This increase also varies latitudinally, roughly decreasing from north to south, with more than 100% at  $39^\circ\text{S}$  but only 18% at  $55^\circ\text{S}$ . As a consequence, since the total energy input (dark red and blue lines in Figure 7a) is dominated by the nonzero frequencies, from summer to winter, the total input

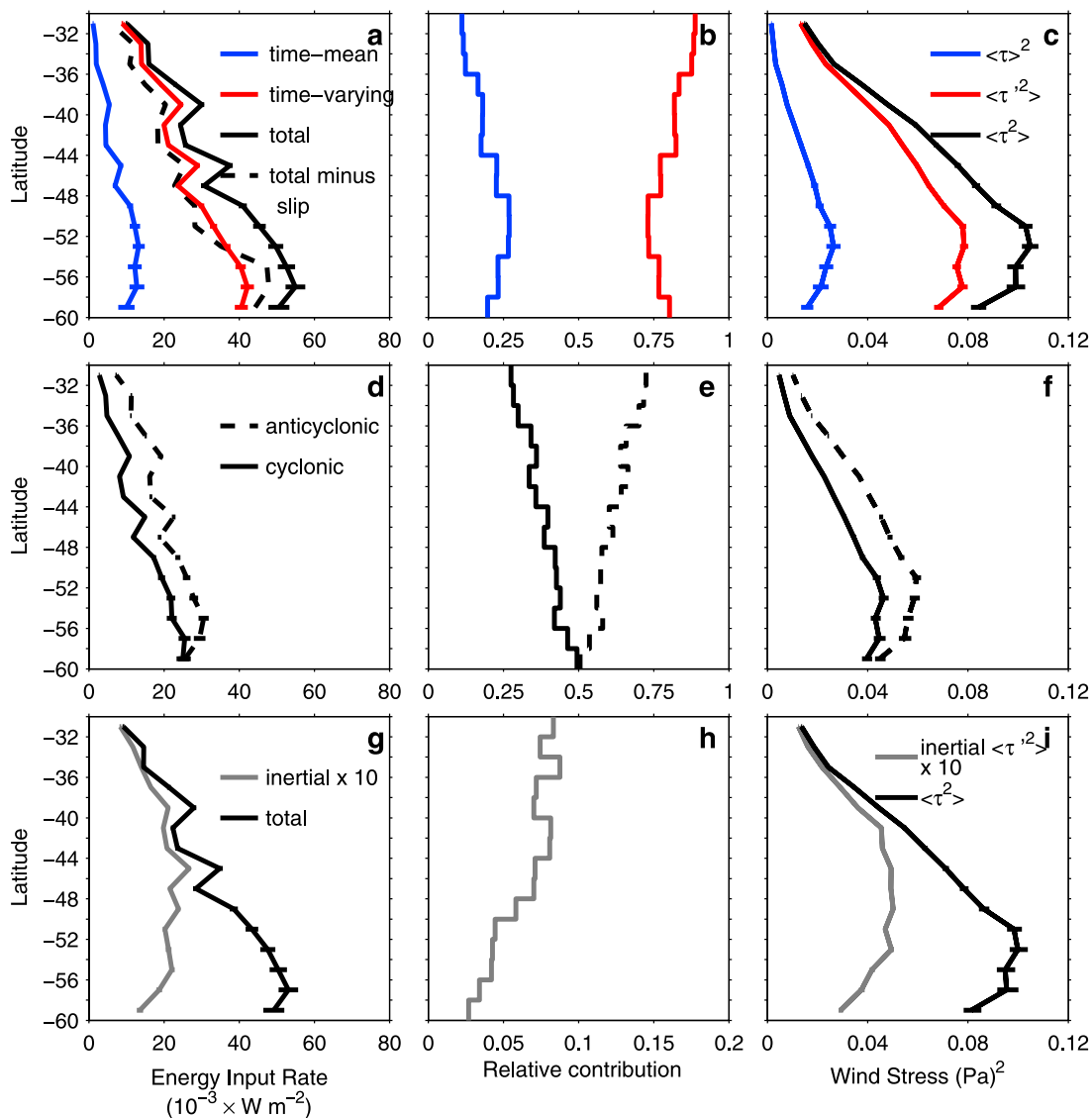


**Figure 6.** Energy input rates across the Southern Ocean. (a) Contributions from the mean, the nonzero frequencies, and total within each latitudinal band. (b) Relative contributions of the zero frequency and of the nonzero frequencies in the total energy input rate. (c) Mean value square, variance, and mean square value of the wind stresses interpolated on the drifter positions. (d) Energy input rate contributions from the anticyclonic and the cyclonic frequencies. (e) Relative contribution of the anticyclonic and cyclonic frequencies for the total energy input rate. (f) Mean square value (variance plus half of the mean) of the wind stresses for anticyclonic and cyclonic frequencies. (g) Contribution from the near-inertial frequencies multiplied by 10 for legibility and contribution from the remaining frequencies. (h) Relative contribution of the near-inertial frequencies for the total energy input rate. Note the change of scale for the abscissa compared to Figures 6b and 6e. (i) Wind stress variance for the near-inertial frequencies multiplied by 10 for legibility and mean square value for the remaining frequencies. Error bars for the energy input rate are derived from the standard errors for the cospectra. Error bars for the wind stress variance are derived from the formal 95% confidence intervals of the wind stress spectra.

also increases on average by approximately 68%, but this seasonal increase varies greatly: south of 42°S it averages 43%, but north of 42°S it averages 106%.

[49] Although the total energy input changes seasonally, the partitioning between anticyclonic and cyclonic components does not. Figures 7d, 7e, and 7f indicate no qualitative differences as a function of seasons.

[50] The wind energy input in the near-inertial range (Figure 7g) does show an increase from summer to winter, between 10% and 118% across the Southern Ocean. This pattern follows the trend of increased wind stress variance in winter in the near-inertial band, but it is less dramatic since the near-inertial variance of the wind stress can be multiplied by a factor up to 2.5. As noted earlier, results

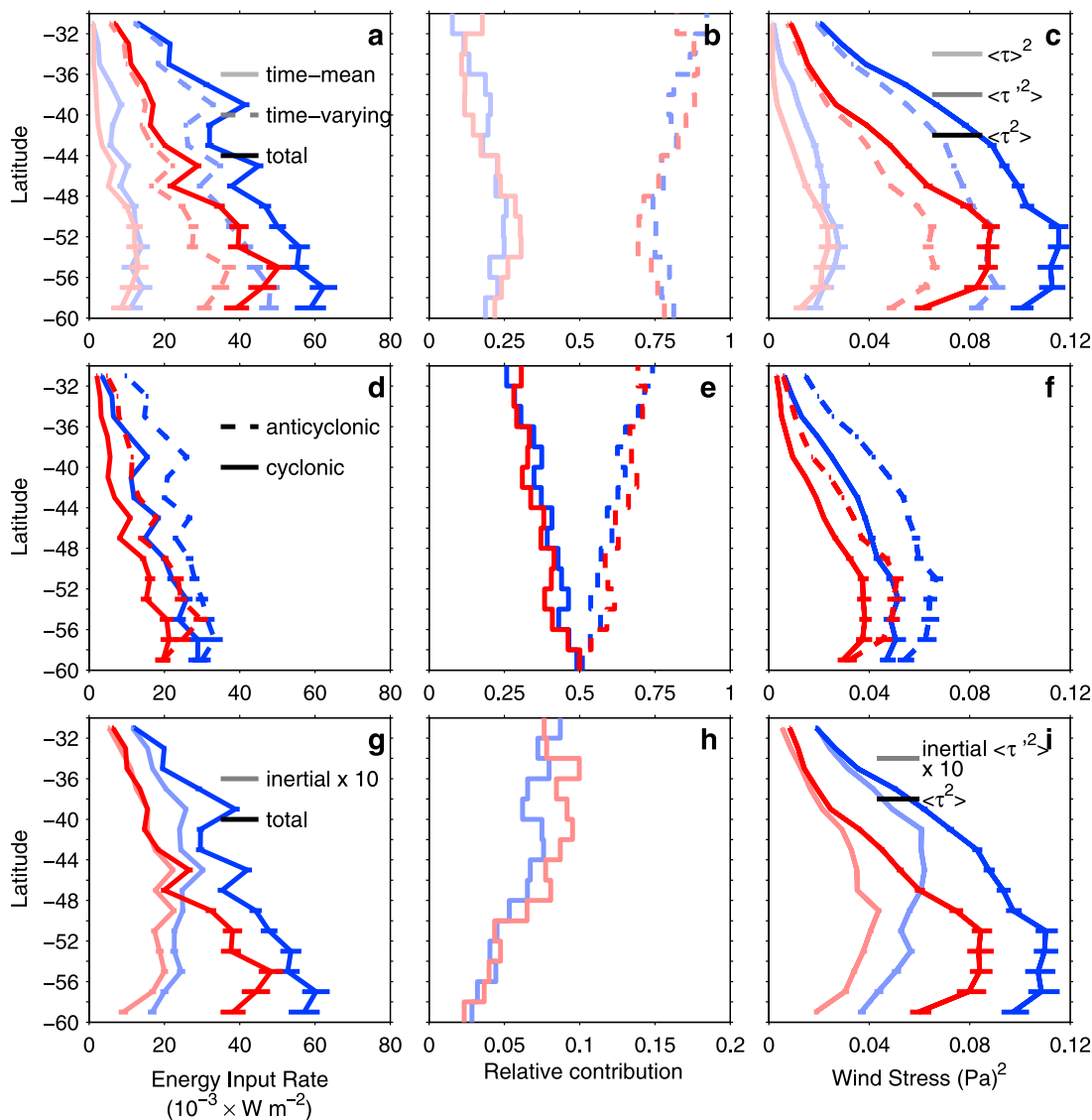


**Figure 7.** As in Figure 6 but for energy input rates across the Southern Ocean as a function of season. Blue shading indicates austral winter, and red shading indicates austral summer.

about the near-inertial range should be considered with caution.

## 6. Summary and Concluding Remarks

[51] A classic diffusion model, in which the turbulent stress is proportional to the vertical shear of the horizontal velocity, is used in the horizontal momentum balance equation of the ocean in the absence of large-scale pressure gradients in order to derive a spectral energy equation. In this framework, the real part of the cross spectrum between the atmospheric stress upon the ocean and the surface ocean velocity is a measure as a function of frequency of the energy input “to the Ekman layer”. This energy is dissipated throughout the depth of the oceanic boundary layer but if passed below it could be an important potential contributor to the mechanical energy budget of the ocean.

[52] Surface drifter data, altimeter data, and reanalysis wind stresses are used to estimate first the zonally averaged

cross spectrum between the wind stress and 15-m ageostrophic velocities for absolute frequencies of motions between 0 and 2 cpd, in the Southern Ocean. Because drifters measure velocities at 15 m depth and not at the surface, some knowledge of the vertical structure of the transfer function is needed to obtain the cross spectrum at the surface. The results from *Elipot and Gille* [2009] are used to infer the cross spectrum at the surface and therefore to estimate the wind energy input to the Ekman layer in this region.

[53] The spectral characteristics of this energy input are studied. Results show that the combination of a stronger anticyclonic wind stress forcing associated with a greater anticyclonic response makes the contribution from the anticyclonic frequencies dominate the wind energy input, providing a potential explanation for the predominance of anticyclonic motions at these latitudes.

[54] The latitudinal and seasonal variations of the wind energy input to the Ekman layer are closely related to the

variations of the wind stress, for the mean and for the time-varying components. From these, the contribution from the near-inertial band follows a different trend, increasing from low latitudes to about 45°S, and decreasing further south.

[55] The uncertainties arising from the drifter data could substantially modify our quantitative results. In particular the effect of the wind slip could lower our estimates by 27% on average. It is therefore crucial to understand better the behavior of surface drifters in high-wind and high-wave environments such as in the Southern Ocean. However, we argue here that surface drifter velocities can be used to obtain global estimates of the wind energy input to the Ekman layer, provided that we obtain a good understanding of vertical viscosity and boundary layer depth so that the surface cross spectrum can be obtained from the 15 m cross spectrum. This is of potential great importance as nonzero-frequency forcing of the ocean is related to the sources of kinetic energy in the form of internal waves that are related to the mixing of the ocean.

[56] The somewhat modest contribution of the near-inertial frequency range to the wind energy input to the Ekman layer seems at odds with the general thinking that most of the wind energy that is deposited in the upper ocean is through processes at near-inertial frequencies such as the ones described by a slab-layer model [e.g., Alford, 2003b].

[57] First, as mentioned earlier, there is a clear lack of near-inertial variance in both the data sets used here: the historical kriged drifter data set [Chaigneau et al., 2008; Elipot and Lumpkin, 2008] and the reanalysis winds [Gille, 2005]. In fact, the near-inertial variance in the unkriged drifter data set has recently been shown to be larger [Chaigneau et al., 2008; Elipot and Lumpkin, 2008] than what we observe here or in previous studies [e.g., Rio and Hernandez, 2003]. Thus the contribution from near-inertial frequencies is likely underestimated with the data sets used for this study, in particular for the latitudes poleward of 45°S. Quantifying the impact on our results that would have the use of higher-temporal-resolution drifter velocity data is difficult because high-frequency variance in the wind data would still be lacking.

[58] Secondly, we have considered the results of the cross-spectral analysis only in the framework of Ekman dynamics. This is particularly important for the frequency-dependent shear correction applied here, from the results of Elipot and Gille [2009], that aims at ameliorating the fact that drifter velocities are at 15 m depth and not at the surface. Modeling oscillations in the mixed layer by a slab-layer model is a very different approach because in that case uniformity of the currents in the vertical is assumed, which is most likely not the proper model for subinertial oceanic oscillations [Weller and Plueddemann, 1996; Elipot and Gille, 2009]. Also, Rio and Hernandez [2003] showed for all latitudes that the coherence between kriged drifter velocity data and reanalyses winds drops at frequencies exceeding the inertial frequency and not only at the relatively high latitudes of the Southern Ocean. This implies that the cospectrum, and hence the wind energy input through the linear approach utilized here is dramatically reduced as one approaches the inertial frequency. This clearly calls for further research to reconcile the subinertial Ekman-type of forcing presented here and the slab-forced model at near-inertial frequencies.

[59] **Acknowledgments.** We thank Glenn Ierley, Peter Niiler, and Bruce Cornuelle for their valuable advice. This research was supported by the National Science Foundation under grant OCE-9985203/OCE-0049066; by the NASA Ocean Vector Wind Science Team, JPL contract 1222984; and by the NASA Ocean Surface Topography Science Team, JPL Contract 1224031.

## References

- Alford, M. H. (2001), Internal swell generation: The spatial distribution of energy flux from the wind to mixed layer near-inertial motions, *J. Phys. Oceanogr.*, *31*, 2359–2368.
- Alford, M. H. (2003a), Improved global maps and 54-year history of wind-work on ocean inertial motions, *Geophys. Res. Lett.*, *30*(8), 1424, doi:10.1029/2002GL016614.
- Alford, M. H. (2003b), Redistribution of energy available for ocean mixing by long-range propagation of internal waves, *Nature*, *423*, 159–162.
- Alford, M. H., and M. Whitmont (2007), Seasonal and spatial variability of near-inertial kinetic energy from historical moored velocity records, *J. Phys. Oceanogr.*, *37*, 2022–2037.
- Bendat, J. S., and A. G. Piersol (1986), *Random Data: Analysis and Measurements Procedures*, 3rd ed., 594 pp., John Wiley, New York.
- Centre National d'Etudes Spatiales (1996), AVISO user handbook for merged TOPEX/POSEIDON products, Rep. AVI-NT-02-101-CN, Ramonville-Saint-Agne, France.
- Chaigneau, A., O. Pizarro, and W. Rojas (2008), Global climatology of near-inertial current characteristics from Lagrangian observations, *Geophys. Res. Lett.*, *35*, L13603, doi:10.1029/2008GL034060.
- Chiu, W.-C. (1970), On the spectral equations and the statistical energy spectrum of atmospheric motions in the frequency domain, *Tellus*, *22*, 608–619.
- Crawford, G. B., and W. G. Large (1996), Numerical investigation of resonant inertial response of the ocean to wind forcing, *J. Phys. Oceanogr.*, *26*, 873–891.
- D'Asaro, E. A. (1985a), The energy flux from the wind to near-inertial motions in the surface mixed layer, *J. Phys. Oceanogr.*, *15*, 1043–1059.
- D'Asaro, E. A. (1985b), Upper ocean temperature structure, inertial currents, and Richardson numbers observed during strong meteorological forcing, *J. Phys. Oceanogr.*, *15*, 943–962.
- D'Asaro, E. A., C. C. Eriksen, M. D. Levine, P. Niiler, C. A. Paulson, and P. Van Meurs (1995), Upper-ocean inertial currents forced by a strong storm. Part I: Data and comparisons with linear theory, *J. Phys. Oceanogr.*, *25*, 2909–2936.
- Duhaut, T. H. A., and D. N. Straub (2006), Wind stress dependence on ocean surface velocity: Implications for mechanical energy input to ocean circulation, *J. Phys. Oceanogr.*, *36*, 202–211.
- Ekman, V. W. (1905), On the influence of the Earth's rotation on ocean currents, *Ark. Mat. Astron. Fys.*, *2*(11), 1–36.
- Elipot, S. (2006), Spectral characterization of Ekman velocities in the Southern Ocean based on surface drifter trajectories, Ph.D. thesis, Scripps Inst. of Oceanogr., Univ. of Calif., San Diego.
- Elipot, S., and S. T. Gille (2009), Ekman layers in the Southern Ocean: Spectral models and observations, vertical viscosity and boundary layer depth, *Ocean Sci. Discuss.*, *6*(1), 277–341.
- Elipot, S., and R. Lumpkin (2008), Spectral description of oceanic near-surface variability, *Geophys. Res. Lett.*, *35*, L05606, doi:10.1029/2007GL032874.
- Ferrari, R., and C. Wunsch (2008), Ocean circulation kinetic energy: Reservoirs, sources and sinks, *Annu. Rev. Fluid Mech.*, *41*, 253–282.
- Fofonoff, N. P. (1981), The Gulf Stream, in *Evolution of Physical Oceanography: Scientific Surveys in Honor of Henry Stommel*, edited by B. A. Warren and C. Wunsch, pp. 112–139, MIT Press, Cambridge, Mass.
- Gill, A. E. (1984), On the behavior of internal waves in the wakes of storms, *J. Phys. Oceanogr.*, *14*, 1129–1151.
- Gill, A. E., J. S. A. Green, and A. Simmons (1974), Energy partition in the large-scale ocean circulation and the production of mid-ocean eddies, *Deep Sea Res. Oceanogr. Abstr.*, *21*, 499–528.
- Gille, S. T. (2005), Statistical characterization of zonal and meridional ocean wind stress, *J. Atmos. Oceanic Technol.*, *22*, 1353–1372.
- Gonella, J. (1972), A rotary-component method for analysing meteorological and oceanographic vector time series, *Deep Sea Res. Oceanogr. Abstr.*, *19*, 833–846.
- Gregg, M. C. (1987), Diapycnal mixing in the thermocline: A review, *J. Geophys. Res.*, *92*, 5249–5286.
- Griffa, A.-L., R. Lumpkin, and M. Veneziani (2008), Cyclones and anticyclones in the upper ocean: From large eddies to submesoscales, *Geophys. Res. Lett.*, *35*, L01608, doi:10.1029/2007GL032100.
- Hansen, D. V., and P.-M. Poulain (1996), Quality control and interpolations of WOCE-TOGA drifter data, *J. Atmos. Oceanic Technol.*, *13*, 900–909.
- Huang, R. X., W. Wei, and L. L. Liu (2006), Decadal variability of wind-energy input to the world, *Deep Sea Res., Part II*, *53*, 31–41.

- Hughes, C., and C. Wilson (2008), Wind work on the geostrophic ocean circulation: An observational study of the effect of small scales in the wind stress, *J. Geophys. Res.*, *113*, C02016, doi:10.1029/2007JC004371.
- Large, W. G., J. C. McWilliams, and S. C. Doney (1994), Oceanic vertical mixing: A review and a model with a nonlocal boundary layer parameterization, *Rev. Geophys.*, *32*, 363–404.
- Lumpkin, R., and P. Flament (2001), Lagrangian statistics in the central North Pacific, *J. Mar. Syst.*, *29*, 141–155.
- Lumpkin, R., and M. Pazos (2007), Measuring surface currents with SVP drifters: The instrument, its data, and some recent results, in *Lagrangian Analysis and Prediction of Coastal and Ocean Dynamics*, edited by A. Griffa et al., pp. 39–67, Cambridge Univ. Press, New York.
- McNally, G. J., D. S. Luther, and W. B. White (1989), Subinertial frequency response of wind-driven currents in the mixed layer measured by drifting buoys in the midlatitude North Pacific, *J. Phys. Oceanogr.*, *19*, 290–300.
- Niiler, P. P., and J. D. Paduan (1995), Wind-driven motions in the northeast Pacific as measured by Lagrangian drifters, *J. Phys. Oceanogr.*, *25*, 2819–2830.
- Niiler, P. P., A. L. Sybrandy, K. Bi, P. Poulain, and D. Bitterman (1995), Measurements of the water-following capability of holey-sock and TRISTAR drifters, *Deep Sea Res., Part 1*, *42*, 1951–1964.
- Niiler, P. P., N. A. Maximenko, and J. C. McWilliams (2003), Dynamically balanced absolute sea level of the global ocean derived from near-surface velocity observations, *Geophys. Res. Lett.*, *30*(22), 2164, doi:10.1029/2003GL018628.
- Plueddemann, A. J., and J. T. Farrar (2006), Observations and models of the energy flux from the wind to mixed-layer inertial currents, *Deep Sea Res., Part II*, *53*, 5–30.
- Pollard, R. T., and R. C. J. Millard (1970), Comparison between observed and simulated wind-generated inertial oscillations, *Deep Sea Res. Oceanogr. Abstr.*, *17*, 813–821.
- Polton, J. A., J. A. Smith, J. A. MacKinnon, and A. E. Tejada-Martinez (2008), Rapid generation of high-frequency internal waves beneath a wind and wave forced oceanic surface mixed layer, *Geophys. Res. Lett.*, *35*, L13602, doi:10.1029/2008GL033856.
- Poulain, P.-M. (1990), Near-inertial and diurnal motions in the trajectories of mixed layer drifters, *J. Mar. Res.*, *48*, 793–823.
- Poulain, P.-M., D. S. Luther, and W. C. Patzert (1992), Deriving inertial wave characteristics from surface drifter velocities: Frequency variability in the tropical Pacific, *J. Geophys. Res.*, *97*, 17,947–17,959.
- Rio, M. H., and F. Hernandez (2003), High-frequency response of wind-driven currents measured by drifting buoys and altimetry over the world ocean, *J. Geophys. Res.*, *108*(C8), 3283, doi:10.1029/2002JC001655.
- Rudnick, D. L., and R. A. Weller (1993), Observations of superinertial and near-inertial wind-driven flow, *J. Phys. Oceanogr.*, *23*, 2351–2359.
- Saji, P. K., S. C. Shenoi, A. Almeida, and G. Rao (2000), Inertial currents in the Indian Ocean derived from satellite tracked surface drifters, *Oceanol. Acta*, *23*, 635–640.
- Simmons, A. J., and J. K. Gibson (2000), The ERA-40 project plan, ERA-40 Proj. Rep. Ser. 1, Eur. Cent. for Medium-range Weather Forecasts, Reading, U. K.
- Stern, M. E. (1975), *Ocean Circulation Physics*, 275 pp., Academic, New York.
- Stockwell, R. G., W. G. Large, and R. F. Milliff (2004), Resonant inertial oscillations in moored buoy ocean surface winds, *Tellus, Ser. A*, *56*, 536–536.
- Tapley, B., et al. (2005), GGM02 — An improved Earth gravity field model from GRACE, *J. Geod.*, *79*, 467–478.
- Von Storch, J. S., H. Sasaki, and J. Marotzke (2007), Wind-generated power input to the deep ocean: An estimate using a 1/10 general circulation model, *J. Phys. Oceanogr.*, *37*, 657–672.
- Wang, W., and R. Huang (2004), Wind energy input to the Ekman layer, *J. Phys. Oceanogr.*, *34*, 1267–1275.
- Watanabe, M., and T. Hibiya (2002), Global estimates of the wind-induced energy flux to inertial motions in the surface mixed layer, *Geophys. Res. Lett.*, *29*(8), 1239, doi:10.1029/2001GL014422.
- Weijer, W., and S. T. Gille (2005), Energetics of wind-driven barotropic variability in the Southern Ocean, *J. Mar. Res.*, *63*, 1101–1125.
- Weller, R. A. (1981), Observations of the velocity response to wind forcing in the upper ocean, *J. Geophys. Res.*, *86*, 1969–1977.
- Weller, R. A., and A. J. Plueddemann (1996), Observations of the vertical structure of the oceanic boundary layer, *J. Geophys. Res.*, *101*, 8789–8806.
- Wunsch, C. (1998), The work done by the wind on the oceanic general circulation, *J. Phys. Oceanogr.*, *28*, 2332–2340.
- Wunsch, C., and R. Ferrari (2004), Vertical mixing, energy, and the general circulation of the oceans, *Annu. Rev. Fluid Mech.*, *36*, 281–314.

S. Elipot, Proudman Oceanographic Laboratory, 6 Brownlow Street, Liverpool L3 5DA, UK. (ship@pol.ac.uk)

S. T. Gille, Scripps Institution of Oceanography, University of California, San Diego, 9500 Gilman Drive, Mail Code 0230, La Jolla, CA 92093-0230, USA.